Supporting Information

In situ Methods for Identifying Reactive Surface Intermediates during Hydrogenolysis Reactions: C-O Bond Cleavage on Nanoparticles of Nickel and Nickel Phosphides

Megan E. Witzke,[†] Abdulrahman Almithn,[§] Christian L. Coonrod,[†] Mark D. Triezenberg,[†] David D. Hibbitts,[§,*] and David W. Flaherty[†,*]

[†]Department of Chemical and Biomolecular Engineering, University of Illinois Urbana-Champaign, Urbana, IL 61801

[§]Department of Chemical Engineering, University of Florida, Gainesville, FL 32611

Table of Contents

List of Tables

List of Figures

S1. Reaction Coordinate Diagrams

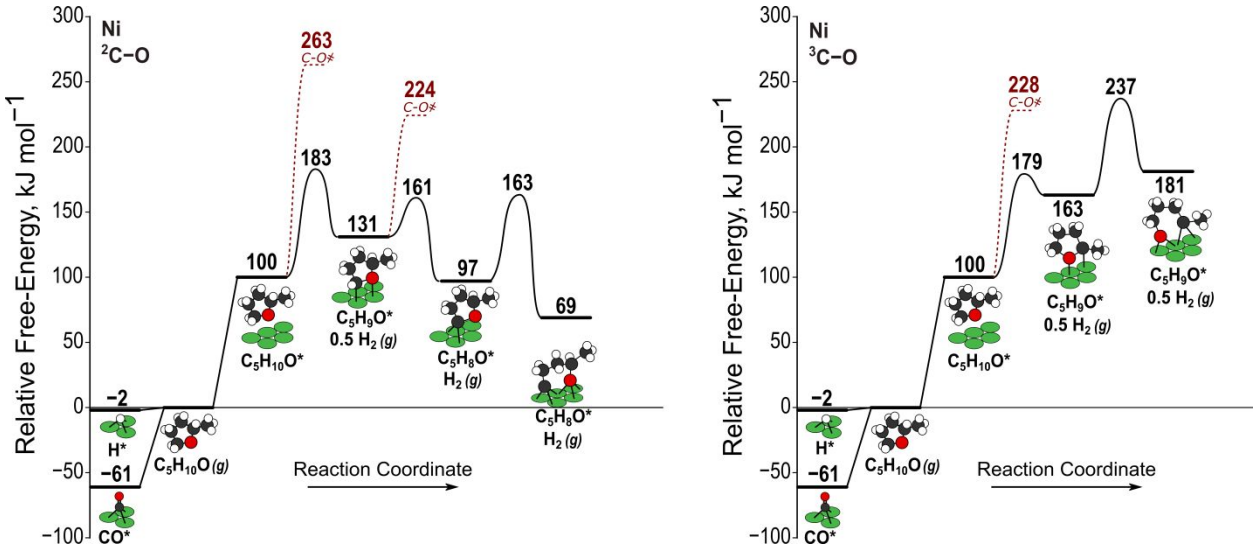

Figure S1 Reaction coordinate diagram for changes in free energy in elementary steps that form the transition state for ^{2}C–O and ^{3}C–O bond rupture in MTHF on a Ni(111) surface at 543 K (O: red; C: black; H: white; Ni: green).

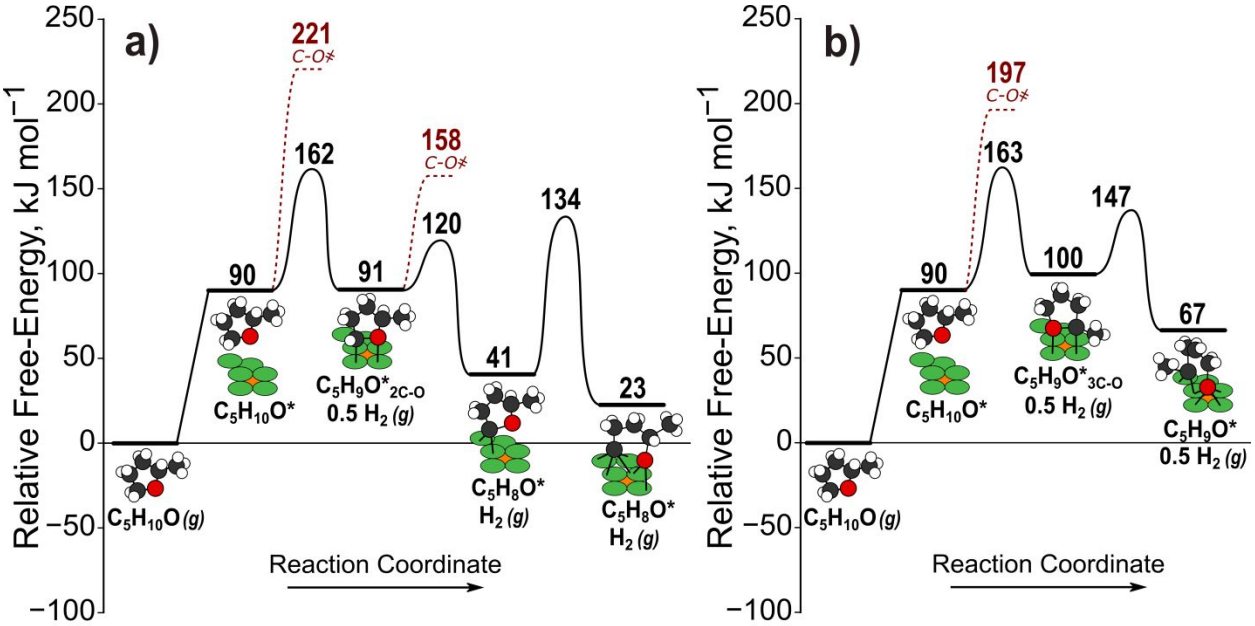

Figure S2 Reaction coordinate diagrams for changes in free energy in elementary steps that form the transition state for ^{2}C–O and ^{3}C–O bond rupture in MTHF on the $Ni_{12}P_5$(001) surface at 543 K (O: red; C: black; H: white; P: orange; Ni: green).

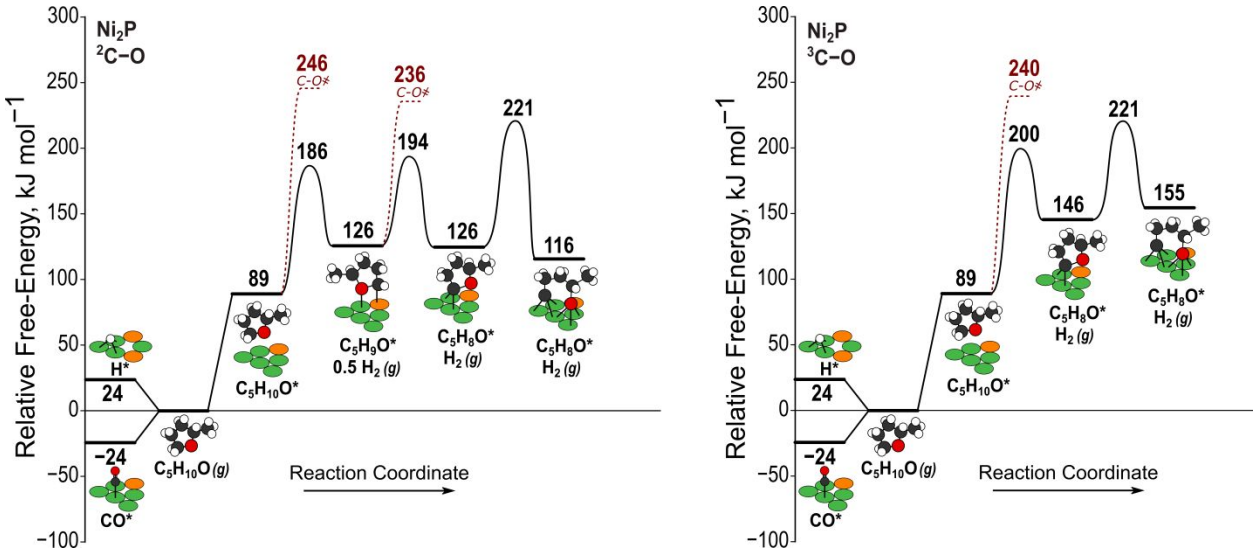

Figure S3 Reaction coordinate diagrams for changes in free energy in elementary steps that form the transition state for ^{2}C–O and ^{3}C–O bond rupture in MTHF on the Ni_2P(001) surface at 543 K (O: red; C: black; H: white; P: orange; Ni: green).

S2. Reference Spectra and Predicted Vibrations for Peak Fitting and Assignments

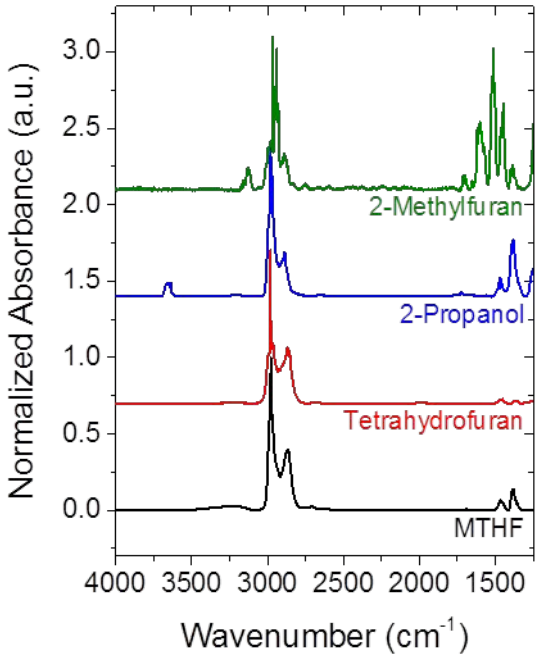

Figure S4 Normalized gas phase spectra of MTHF (black, 12 kPa, 298 K), tetrahydrofuran (red, 9.2 kPa, 328 K), 2-propanol (blue, 9.8 kPa, 328 K), and 2-methylfuran (green, 8.5 kPa, 328 K) measured in an empty gas transmission cell.

Peak of individual vibrational modes are assigned based in part on the peaks present in these pure gas phase spectra. Individual peaks were fit using the Multipeak Fit function with Lorentzian distributions OriginPro to identify and analyze individual ν(C-H) modes of gas phase MTHF, as detailed in Figure S5. The following user defined parameters were used within OriginPro: the distributions are forced to share a common y axis offset; full width at half max (FWHM) is restricted to 0-100 cm^{-1}; peak area is required to be positive; peak finding settings used the 2nd derivative (search hidden peaks) method; peak minimum height was 3% of the y scale; and iteration tolerance was $1*10^{-9}$.

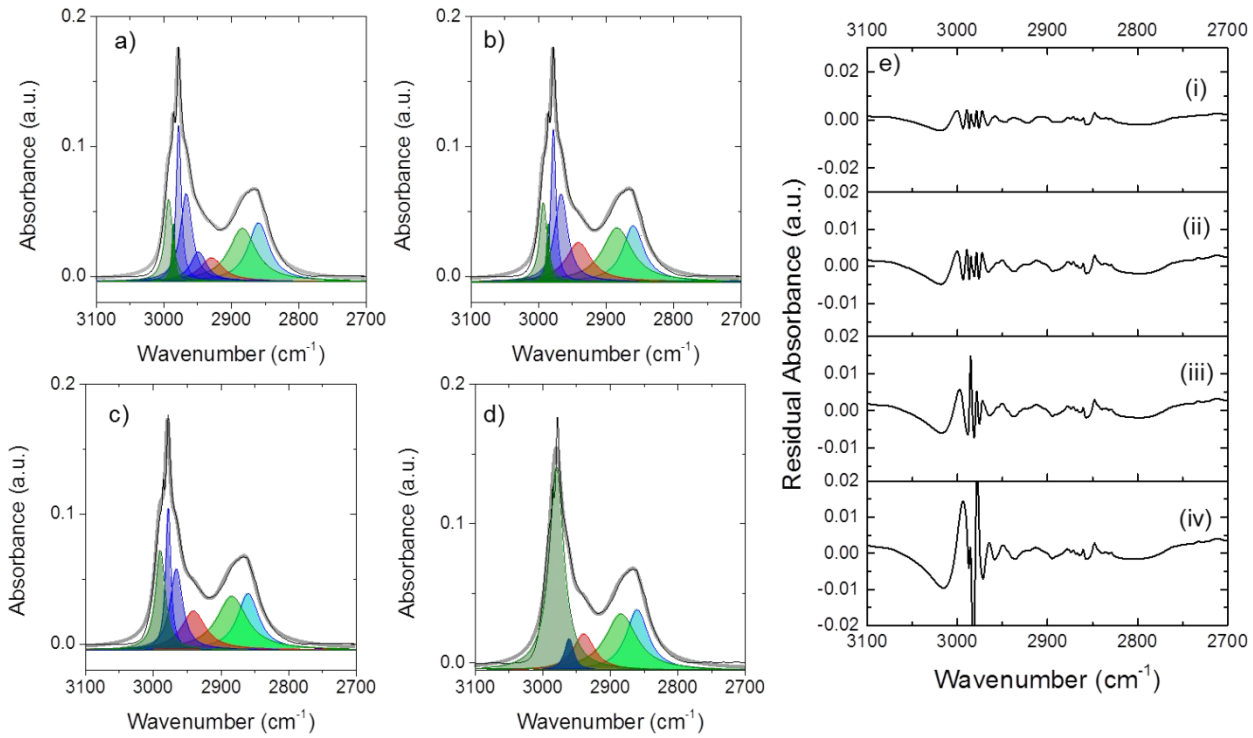

Figure S5 Spectra of gas phase MTHF (12 kPa, 543 K) deconvoluted to peaks (8 peaks, (a); 7 peaks, (b); 6 peaks, (c); 5 peaks, (d)) that represent individual vibrational modes for C-H stretches ($\nu_{CH3,a}$ green; $\nu_{CH3,s}$ light green; $\nu_{CH2,a}$, blue; $\nu_{CH2,s}$, light blue; ν_{CH}, red) which form the cumulative spectra (orange) and e) the residual absorbance between the measured spectra and the cumulative fit to 8 peaks (i), 7 peaks (ii), 6 peaks (iii), and 5 peaks (iv).

The number of peaks fit to a given spectra is based on the fundamental types of vibrational modes within the given wavenumber range. Here, there are 5 basic C-H stretching modes; however, the different methylene groups within MTHF may be electronically different enough to appear as distinct vibrational modes due to their interactions with the catalyst surface (i.e., direct interactions) or based on their proximity to the C-atoms that bind to the catalyst surface (i.e., inductive effects). By increasing the number of peaks, the residuals decreases such that when the measured spectra is fit to 8 peaks, the sharp features ~2975 cm^{-1} are accurately modeled. This process was repeated for each of the isolated reactive intermediates obtained from the phase resolved spectra using MCR-ALS.

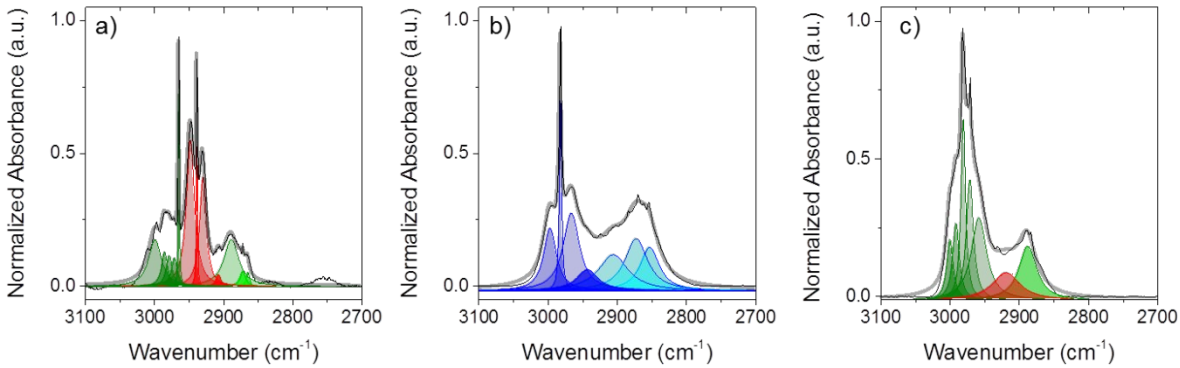

Figure S6 Spectra of gas phase 2-methylfuran (a, 8.5 kPa, 328 K), tetrahydrofuran (b, 9.2 kPa, 328 K), 2-propanol (c, 9.8 kPa, 328 K) measured in an empty gas transmission cell and deconvoluted to peaks the reflect individual C-H stretches ($\nu_a(CH_3)$ green; $\nu_s(CH_3)$ light green; $\nu_a(CH_2)$, blue; $\nu_s(CH_2)$, light blue; ν(CH), red) which form the cumulative spectra (transparent gray).

Table S1 Ratio of absorbance intensity at 2975 cm^{-1} for SiO_2 supported 4 nm Ni, 10 nm $Ni_{12}P_5$, and 12 nm Ni_2P nanoparticles relative to that of SiO_2 during reactions of MTHF for spectra reported in Figure 3 (12 kPa MTHF, 43 kPa H_2, 46 kPa He, 543 K)

Catalyst	Max intensity at ~2975 cm^{-1} (a.u. g^{-1})	Relative ratio with SiO_2
4 nm Ni	0.00617	1.99
10 nm $Ni_{12}P_5$	0.00344	1.11
12 nm Ni_2P	0.00389	1.25
SiO_2	0.0031	1

S3. Steady State Spectra Measured at Multiple Temperatures

Ni, $Ni_{12}P_5$ and Ni_2P surfaces stabilize the reactive intermediates that form during ^{3}C-O and ^{2}C-O bond rupture differently based on the relative free energies (ΔG) (Figures S1-S3); therefore, the coverage of each intermediate should respond uniquely to changes in temperature. Additionally, species with the same composition may change orientation with temperature without changing composition, as noted in previous works that observe the rotation of C_6-hydrocarbons from hexylidyne in all trans to gauche-trans-trans configuration over Pt,[1,2] and Ru[3] with increased temperature. Spectra obtained at steady state as a function of temperature (400-600 K; Figure S7) over SiO_2 supported 4 nm Ni, 10 nm $Ni_{12}P_5$, and 12 nm Ni_2P clusters reveal significant changes with increasing temperature in spectral features attributed to the ν(C-H). The features at ~2940 cm^{-1} that represent the asymmetric perturbed methylene stretch ($\nu_{ap}(CH_2)$) based on gas phase spectra (Figures S5 and S6) and previous literature[1,3-6] decreases with increasing temperature relative to the unperturbed $\nu_a(CH_2)$ (2960 cm^{-1}) over Ni, $Ni_{12}P_5$, and Ni_2P surfaces. The decrease in relative intensity of $\nu_{ap}(CH_2)$ to $\nu_a(CH_2)$ with increasing temperature indicates that methylene groups as a whole (from spectators and reactive intermediates) are farther from the catalyst surface at higher temperatures. The asymmetric methyl stretch ($\nu_{CH3,a}$(C-H)) red shifts from 2990 cm^{-1} to become a shoulder near 2985 cm^{-1} with increasing temperature, which indicates the methyl group approaches the surface with increasing temperature. The ratio of asymmetric (2990-2960 cm^{-1}) to symmetric (2880-2850 cm^{-1}) methylene and methyl groups increases with increasing temperature, which indicates the plane of the furan ring changes orientation relative to the Ni, $Ni_{12}P_5$, and Ni_2P surfaces such that the net z component of the C-H bonds in methyl and methylene groups is non-zero relative to the catalyst surface in the xy-plane. Figure S8 illustrates two orientations of MTHF relative to a catalyst surface in which the orientation in Figure S8b would demonstrate a greater ratio of ν_a(C-H) to ν_s(C-H) relative to Figure S7a. Previous in situ IR spectra of MTHF in H_2 over SiO_2 supported Ni_2P nanoparticles also show a similar red shift in $\nu_{CH3,a}$(C-H), and changing ratio of both $\nu_{CH2,ap}$(C-H) to $\nu_{CH2,a}$(C-H) and ν_a(C-H) to ν_s(C-H) as reported here within a narrower temperature range (448-598 K).[7] Comparisons with spectra of MTHF in N_2 over Ni_2P nanoparticles reveal greater ratios of $\nu_{ap}(CH_2)$ (2936 cm^{-1}) with co-fed H_2, which the authors propose results from the formation of pentalkoxide, a surface intermediate following ^{3}C-O bond rupture;[7] however, this work does not account for contributions from spectators that may form during the rapid H-transfer within MTHF-derived intermediates. Isolation of spectra from individual reactive intermediates and their concentrations without spectator species will provide a clear description of how temperature changes the coordination and relative concentrations of reactive species across different catalyst surfaces during hydrogenolysis reactions.

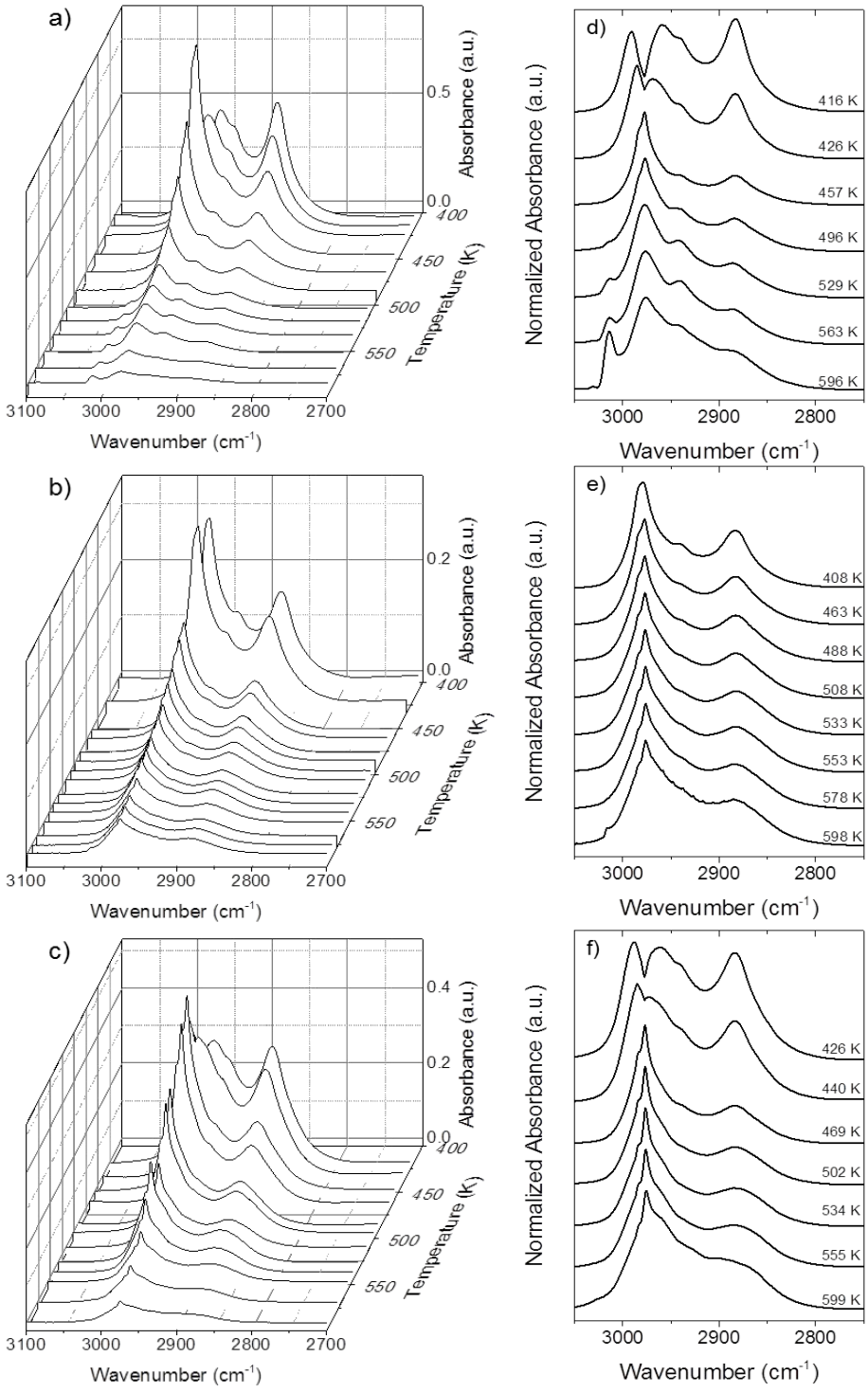

Figure S7 Infrared spectra obtained at several temperatures in situ during steady-state reactions of MTHF and H_2 over SiO_2 supported catalysts including 4 nm Ni (a,d), 10 nm $Ni_{12}P_5$ (b,e), 12 nm Ni_2P (c,f) (5 kPa MTHF, 81 kPa H_2, 15 kPa He, 543 K). (d-f) Spectra normalized by the maximum intensity at ~2975 cm^{-1}.

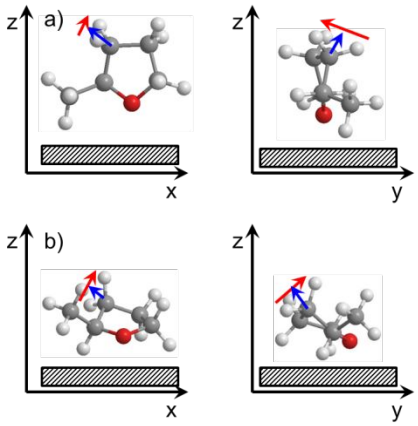

Figure S8. Illustrations of different orientations of MTHF relative to a catalyst surface. Arrows indicate the net vector for dipole movement of a $\nu_{CH2,a}$(C-H) (red) and $\nu_{CH2,s}$(C-H) (blue). C, grey; O, red; H, white.

The spectra over Ni and Ni_2P (Figures S7a, S7c, S7d and S7f) at the lowest temperatures show a more significant shift in the $\nu_{CH3,a}$(C-H) to higher wavenumbers and $\nu_a(CH_2)$ to lower wavenumbers in comparison with $Ni_{12}P_5$ (Figures S7b and S7e), which indicates the composition and orientation of MTHF-derived intermediates on $Ni_{12}P_5$ are less sensitive to temperature changes compared with intermediates over Ni and Ni_2P perhaps as a result of lower ΔG values. DFT calculations predict lower ΔG values for reactive intermediates that lead to C-O bond rupture in MTHF over $Ni_{12}P_5$(001) (Figure S2) compared with Ni_2P(001) (Figure S3) and Ni(111) (Figure S1); however, we cannot distinguish changes in coverage from changes in orientation as these steady state spectra include contributions from spectator species that form from rapid H-transfer.

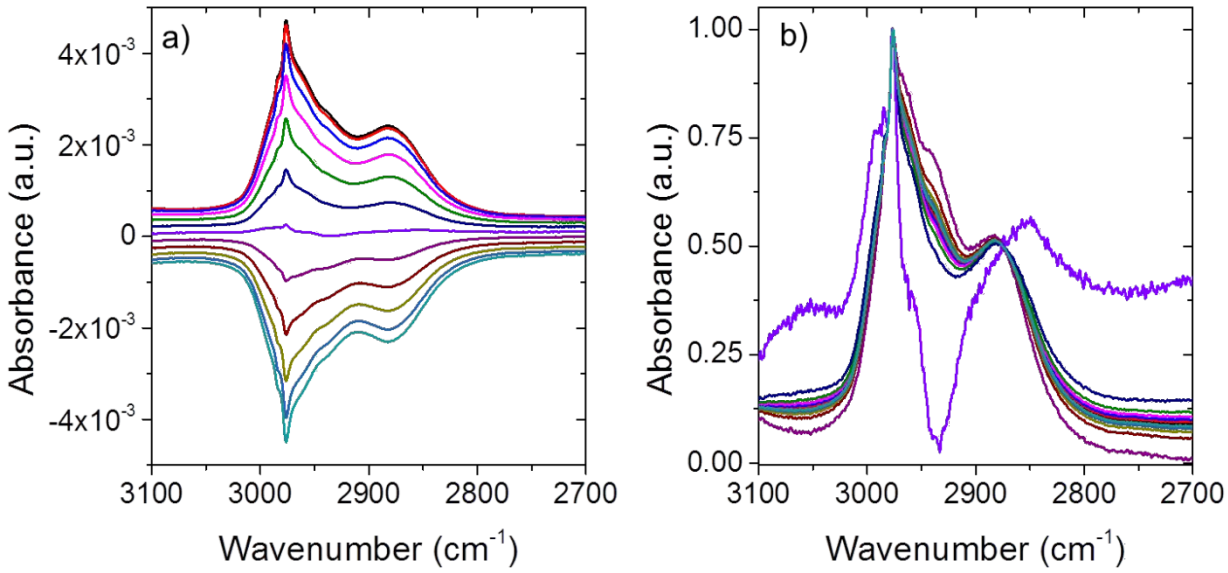

Figure S9. a) Resampled phase resolved spectra (ψ = 1-180°) from the time domain spectra shown in Figure 1a measured during reaction of MTHF over 10 nm $Ni_{12}P_5$ with H_2 pressure modulated over a period of 1200 s (12 kPa MTHF, 2.5 – 84 kPa H_2, 543K.) b) Spectra shown in Figure S9a normalized by the absorbance at 2976 cm^{-1}. Colors correspond to every 15° and are consistent between Figure S9a and S9b.

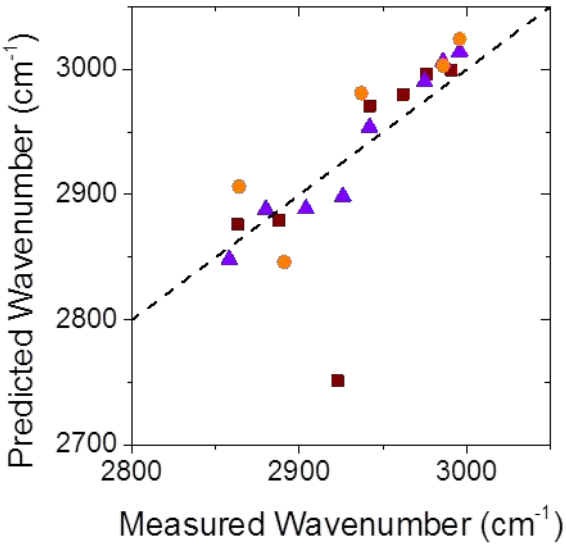

Figure S10 Parity plot of DFT calculated vibrations and measured vibrations of individual ν(C-H) deconvoluted by peak fitting isolated reactive intermediates ($C_5H_{10}O$*, (■); $C_5H_9O^*_{2C\text{-}O}$, (▲); $C_5H_9O^*_{3C\text{-}O}$, (●)) over 10 nm $Ni_{12}P_5$ from extracted from phase resolved spectra using MCR-ALS (12 kPa MTHF, 2.5-84 kPa H_2, 543 K). Asymmetric stretches for DFT predicted vibrations are corrected by 0.985 and symmetric stretches are corrected by 0.967.

Table S2. Vibrational modes for the reactive intermediate ($C_5H_{10}O^*$) measured over 10 nm $Ni_{12}P_5$ (12 kPa MTHF, 2.5-84 kPa H_2, 1200 s period) and predicted* over $Ni_{12}P_5$(001) at 543 K.

Mode	$Ni_4(\eta^5\text{-}C_5H_{10}O^*)$					
	Wavenumber (cm^{-1})					
	Measured[a]	RPBE	optB88-vdW	optB86b-vdW	RPBE-D3BJ	vdW-DF2
$\nu_a(CH_3)$		3048 (3002)	3025 (2980)	3019 (2974)	3062 (3016)	3029 (2984)
	2991	3045 (2999)	3011 (2966)	3009 (2964)	3056 (3010)	3018 (2973)
$\nu_a(CH_3)$ and $\nu_a(CH_2)$	2976	3042 (2996)	3009 (2964)	3005 (2960)	3053 (3007)	3014 (2969)
$\nu_a(CH_2)$	2962	3026 (2980)	2996 (2951)	2992 (2947)	3034 (2988)	3006 (2961)
$\nu_{ap}(CH_2)$	2942	3016 (2971)	2981 (2936)	2975 (2930)	3025 (2980)	2998 (2953)
ν(CH)	2923	2793 (2751)	2719 (2678)	2721 (2680)	2833 (2791)	2709 (2668)
ν(CH)						
$\nu_s(CH_3)$	2888	2976 (2879)	2950 (2853)	2954 (2857)	2984 (2886)	2958 (2860)
$\nu_s(CH_3)$ and $\nu_s(CH_2)$		2973 (2876)	2946 (2849)	2949 (2852)	2990 (2891)	2964 (2866)
$\nu_s(CH_2)$	2863	2973 (2876)		2942 (2845)		
		3000 (2836)	2963 (2865)		3010 (2911)	2980 (2882)

*Values shown between parenthesis are the corrected vibrations (by 0.985 for asymmetric vibrations and 0.967 for symmetric vibrations).

Table S3. Vibrational modes for the reactive intermediate ($C_5H_9O^*$) measured over 10 nm $Ni_{12}P_5$ (12 kPa MTHF, 2.5-84 kPa H_2, 1200 s period) and predicted* over $Ni_{12}P_5$(001) at 543 K.

Mode	$Ni_2(\mu^2\text{-}C_5H_9O^*)_{2C\text{-}O}$					
	Wavenumber (cm^{-1})					
	Measured[a]	RPBE	optB88-vdW	optB86b-vdW	RPBE-D3BJ	vdW-DF2
$\nu_a(CH_3)$	2996	3060 (3014)	3012 (2967)	3008 (2963)	3058 (3012)	3013 (2968)
	2986	3052 (3006)	3004 (2959)	3001 (2956)	3050 (3004)	3012 (2967)
$\nu_a(CH_3)$ and $\nu_a(CH_2)$						
$\nu_a(CH_2)$	2975	3036 (2990)	2974 (2929)	2973 (2928)	2977 (2932)	3005 (2960)
	2963					
$\nu_{ap}(CH_2)$	2942	2999 (2954)	2942 (2898)			2981 (2936)
ν(CH)	2926	2943 (2899)	2929 (2885)	2935 (2891)	2997 (2952)	2937 (2893)
ν(CH)	2904	2933 (2889)	2904 (2860)	2903 (2859)	2946 (2902)	2921 (2877)
$\nu_s(CH_3)$	2880	2985 (2888)	2937 (2840)	2920 (2824)	2908 (2812)	2957 (2859)
		2981 (2884)				
$\nu_s(CH_3)$ and $\nu_s(CH_2)$						
$\nu_s(CH_2)$	2858	2944 (2848)	2905 (2809)	2903 (2807)	2910 (2814)	2943 (2846)

*Values shown between parenthesis are the corrected vibrations (by 0.985 for asymmetric vibrations and 0.967 for symmetric vibrations).

Table S4. Vibrational modes for the reactive intermediate (C_5H_9O*) measured over 10 nm $Ni_{12}P_5$ (12 kPa MTHF, 2.5-84 kPa H_2, 1200 s period) and predicted* over $Ni_{12}P_5$(001) at 543 K.

Mode	$Ni_2(\mu^2\text{-}C_5H_9O^*)_{3C\text{-}O}$					
	Wavenumber (cm^{-1})					
	Measured[a]	RPBE	optB88-vdW	optB86b-vdW	RPBE-D3BJ	vdW-DF2
$\nu_a(CH_3)$						
	2996	3070 (3024)	3006 (2961)	3014 (2969)	3058 (3012)	3020 (2975)
$\nu_a(CH_3)$ and $\nu_a(CH_2)$	2961					
$\nu_a(CH_2)$	2986	3049 (3003)	3022 (2977)	3015 (2970)	3056 (3010)	3022 (2977)
	2976	3027 (2981)	3015 (2970)	3011 (2966)	3048 (3002)	3006 (2961)
$\nu_{ap}(CH_2)$	2937					
ν(CH)						
ν(CH)						
$\nu_s(CH_3)$	2891	2942 (2846)	2892 (2797)	2907 (2811)	2959 (2861)	2913 (2817)
$\nu_s(CH_3)$ and $\nu_s(CH_2)$						
$\nu_s(CH_2)$	2864	3004 (2906)	2971 (2873)	2967 (2869)	2999 (2900)	2961 (2863)

*Values shown between parenthesis are the corrected vibrations (by 0.985 for asymmetric vibrations and 0.967 for symmetric vibrations).

Table S5. Measured* and DFT-predicted vibrational modes for furan.

Furan		Frequency (cm^{-1})					
No	Mode	Exp.*	RPBE	optB88	optB86b	D3BJ	vdW-DF2
1	CH str	3161	3214	3209	3199	3220	3225
2	CH str	3154	3208	3203	3193	3212	3220
3	CH str	3140	3184	3175	3169	3193	3186
4	CH str	3129	3173	3165	3158	3183	3175
5	ip-Ring I	1556	1535	1550	1543	1538	1538
6	ip-Ring II	1491	1459	1467	1465	1464	1454
7	ip-Ring III	1384	1370	1382	1377	1373	1371
8	CH ip-bend	1267	1243	1257	1245	1242	1271
9	CH ip-bend	1180	1160	1172	1171	1158	1136
10	ip-Ring IV	1140	1130	1139	1135	1143	1136
11	CH ip-bend	1066	1061	1069	1069	1081	1038
12	ip-Ring V	1040	1024	1033	1029	1026	1005
13	CH ip-bend	995	984	990	988	987	968
14	ip-Ring VI	873	857	872	865	877	870
15	ip-Ring VII	871	850	866	857	861	861
16	CH op-bend	863	847	864	851	844	858
17	CH op-bend	838	808	824	811	804	821
18	CH op-bend	745	728	726	723	723	726
19	CH op-bend	728	691	701	692	686	690
20	op-Ring I	613	601	609	605	601	597
21	op-Ring II	603	593	602	597	594	594

Ref. Shimanouchi, T., Tables of Molecular Vibrational Frequencies Consolidated Volume I, National Bureau of Standards, 1972, 1-160.

Table S6. Measured* and DFT-predicted vibrational modes for methane.

CH_4		Frequency (cm^{-1})					
No	Mode	Exp.*	RPBE	optB88	optB86b	D3BJ	vdW-DF2
1	Asym str	3019	3084	3069	3065	3086	3062
2	Asym str	3019	3084	3068	3064	3086	3062
3	Asym str	3019	3083	3068	3064	3085	3062
4	Sym str	2917	2969	2971	2957	2972	2981
5	Deform	1534	1517	1522	1516	1519	1555
6	Deform	1534	1517	1521	1516	1518	1554
7	Deform	1306	1295	1304	1295	1295	1344
8	Deform	1306	1295	1304	1295	1295	1344
9	Deform	1306	1294	1303	1294	1294	1343

*Ref. Shimanouchi, T., Tables of Molecular Vibrational Frequencies Consolidated Volume I, National Bureau of Standards, 1972, 1-160.

Table S7. Measured* and DFT-predicted vibrational modes for methanol.

CH_3OH		Frequency (cm^{-1})					
No	Mode	Exp.*	RPBE	optB88	optB86b	D3BJ	vdW-DF2
1	OH str	3681	3770	3773	3754	3777	3710
2	CH_3 d-str	3000	3020	3006	3003	3026	3024
3	CH_3 d-str	2960	3003	2988	2986	3008	3010
4	CH_3 s-str	2844	2942	2939	2930	2948	2964
5	CH_3 d-deform	1477	1469	1476	1468	1470	1505
6	CH_3 d-deform	1477	1441	1448	1440	1443	1478
7	CH_3 s-deform	1455	1433	1444	1434	1433	1463
8	OH bend	1345	1316	1311	1313	1319	1327
9	CH_3 rock	1165	1144	1156	1148	1145	1159
10	CH_3 rock	1060	1054	1063	1058	1059	1064
11	CO str	1033	996	1011	1011	1001	944

*Ref. Shimanouchi, T., Tables of Molecular Vibrational Frequencies Consolidated Volume I, National Bureau of Standards, 1972, 1-160."

S4. Theoretical Coverages of Reactive Intermediates during Modulation of H_2 Pressure

This section describes the methods for calculating model coverages of reactive intermediates during modulation of H_2 pressure, based on the proposed mechanism described in previous works[8] and summarized in Scheme S1.

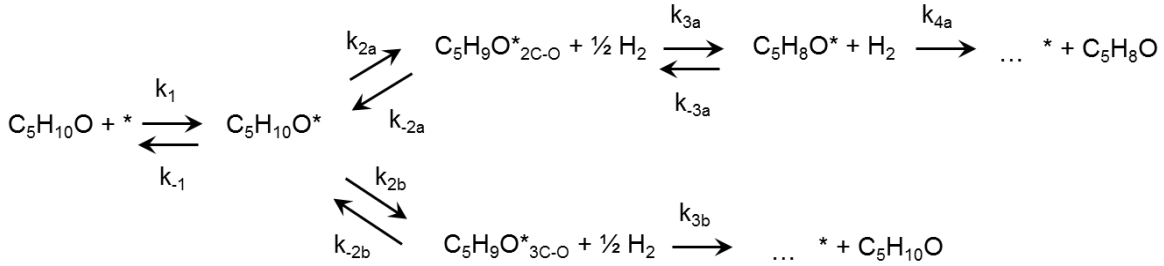

Scheme S1 Proposed mechanism for C-O bond rupture in MTHF over Ni, $Ni_{12}P_5$, and Ni_2P surfaces. Pathways a and b lead to cleavage of the unhindered C-O bond (^{2}C-O) and hindered C-O bond (^{3}C-O), respectively.

We assume differential conversion of reactants based on the mass of catalyst and conditions previously measured in a plug flow reactor;[8] therefore, we assume MTHF pressure is independent of time at 12 kPa. H_2 pressure was modulated in a sinusoidal function:

$$[\mathrm{H_2}] = 40.75 * \sin\left(\frac{t}{T} * 2\pi\right) + 43.25 \tag{S1}$$

Here, $[H_2]$ is H_2 pressure in kPa as a function of time, t, and period length, T. In Figure 4, the period length for modulation is set to 1200 s. The concentrations of reactive intermediates in Scheme S1 are described below:

$$\frac{d[C_5H_{10}O*]}{dt} = k_1[\mathrm{C_5H_{10}O}][*] - k_{-1}[\mathrm{C_5H_{10}O*}] - k_{2a}[\mathrm{C_5H_{10}O*}] - k_{2b}[\mathrm{C_5H_{10}O*}] + k_{-2a}[\mathrm{C_5H_9O*_{^2C-O}}][\mathrm{H_2}]^{\frac{1}{2}} + k_{-2b}[\mathrm{C_5H_9O*_{^3C\text{-}O}}][\mathrm{H_2}]^{\frac{1}{2}} \tag{S2}$$

$$\frac{d[\mathrm{C_5H_9O*_{^2C\text{-}O}}]}{dt} = k_{2a}[\mathrm{C_5H_{10}O*}] - k_{-2a}[\mathrm{C_5H_9O*_{^2C\text{-}O}}][\mathrm{H_2}]^{\frac{1}{2}} - k_{3a}[\mathrm{C_5H_9O*_{^2C\text{-}O}}][H_2]^{\frac{1}{2}} + k_{-3a}[\mathrm{C_5H_8O*}][\mathrm{H_2}]^{\frac{1}{2}} \tag{S3}$$

$$\frac{d[\mathrm{C_5H_8O*}]}{dt} = k_{3a}[C_5H_9O*_{^2C-O}][H_2]^{\frac{1}{2}} - k_{-3a}[C_5H_8O*][H_2]^{\frac{1}{2}} - k_{4a}[C_5H_8O*] \tag{S4}$$

$$\frac{d[\mathrm{C_5H_9O*_{^3C\text{-}O}}]}{dt} = k_{2b}[\mathrm{C_5H_{10}O*}] - k_{-2b}[\mathrm{C_5H_9O*_{^3C\text{-}O}}][\mathrm{H_2}]^{\frac{1}{2}} - k_{3b}[\mathrm{C_5H_9O*_{^3C\text{-}O}}] \tag{S5}$$

The site balance below assumes a constant number of sites:

$$[L] = [*] + [\mathrm{C_5H_{10}O}] + [\mathrm{C_5H_9O*_{^2C\text{-}O}}] + [\mathrm{C_5H_8O*}] + [\mathrm{C_5H_9O*_{^3C\text{-}O}}] \tag{S6}$$

Rate constants were determined using the free energies of reactive intermediates and their transition states calculated by density function theory (Figure S2) but correcting for van der Waals forces in the adsorption of MTHF to the $Ni_{12}P_5$ surface as discussed previously.[8] Table S8 lists the free energies and rate constants used in Figure 4.

Table S8 Intrinsic free energy barriers ($\Delta G^{\ddagger}$) for elementary steps described Scheme S1 and the calculated rate constants for modeled coverages in Figure 4

Elementary Step	$\Delta G^{\ddagger}$ (kJ mol^{-1})	Rate constant (s^{-1})
1	5	$3.74*10^{12}$
-1	50	$1.75*10^{8}$
2a	72	$1.34*10^{6}$
-2a	71	$1.67*10^{6}$
3a	29	$1.83*10^{10}$
-3a	79	$2.84*10^{5}$
4a	47	$3.40*10^{8}$
2b	73	$1.07*10^{6}$
-2b	63	$9.84*10^{6}$
3b	42	$1.03*10^{9}$

Coverages of reactive intermediates and empty sites (*) were calculated as a function of time while modulating [H_2] over 30 periods and solving Equations S1-6 using the rate constants in Table S8 and the ode15s function in MATLAB. Coverages do not respond to the [H_2] in a single sine wave function and we should not expect them to be based on the relative rates of forward and reverse reactions; rather, coverages are described by a Fourier series. Calculated coverages were fit to Fourier series,

$$y_i = y_{i,0} + \sum_{n=1}^{N} \alpha_{i,n} sin\left(2\pi * n \frac{(t - t_{i,n})}{T}\right) \quad \text{(S7)}$$

where y and y_0 are the coverage as a function of time and steady state coverage of species i, α and $t_{i,n}$ are the amplitude and phase shift for each harmonic, n, in the Fourier series calculated to the 5th harmonic (N = 5) for species i.. Figure 4 describes the deviation from the average coverage with respect to the fundamental harmonic (i.e., n = 1) because we set n equal to 1 in Equation 2, thus only apply the first harmonic to the filtering step during phase sensitive detection of the time resolved spectra. Therefore in Figure 4, we plot the sine function,

$$z_i = \alpha_{i,1} sin\left(2\pi * \frac{(t - t_{i,1})}{T}\right) \quad \text{(S8)}$$

where z_i is the deviation from the mean coverage during the simulated modulation of the H_2 pressure.

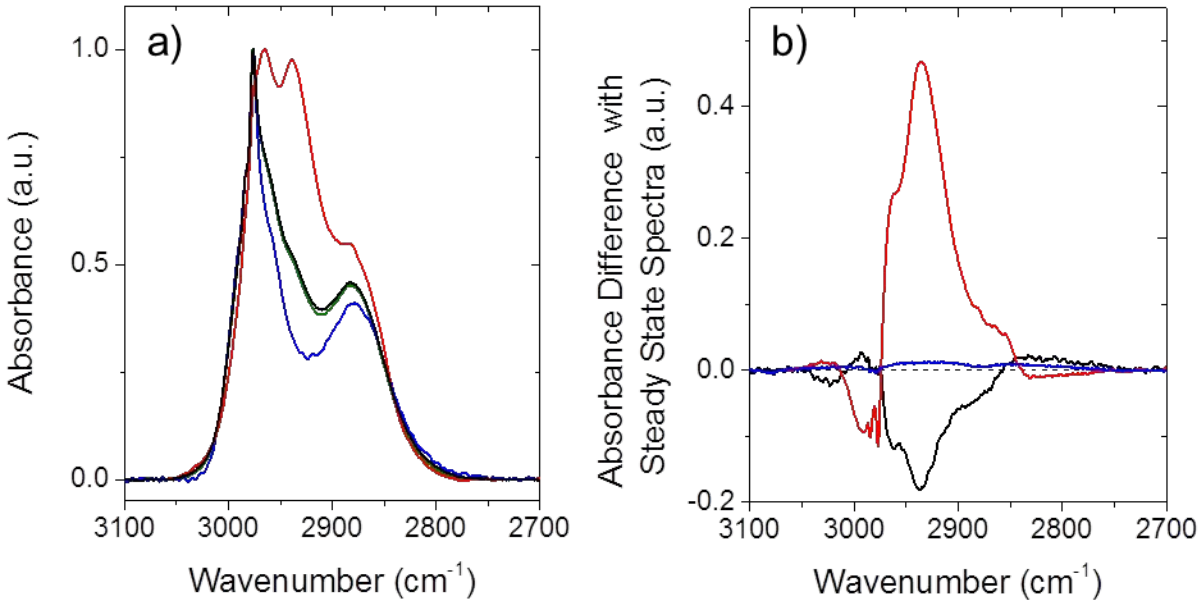

Figure S11 a) Spectra of independent reactive intermediates ($C_5H_{10}O$*, black; C_5H_9O*$_{2C\text{-}O}$, red; C_5H_9O*$_{3C\text{-}O}$, blue) formed during modulation of [H_2] (2.5-84 kPa H_2, 12 kPa MTHF, 543 K, 1200 s) extracted from phase domain spectra using MCR-ALS and spectra obtained at steady state (green, 46 kPa H_2, 12 kPa MTHF, 543 K) over 10 nm $Ni_{12}P_5$. b) Difference in absorbance between the reactive intermediates ($C_5H_{10}O$*, black; C_5H_9O*$_{2C\text{-}O}$, red; C_5H_9O*$_{3C\text{-}O}$, blue) and the steady state spectra. All spectra are baseline corrected and normalized by their maximum intensity near 2976 cm^{-1} prior to calculating the difference in absorbance. Dashed line indicates a value of 0 to guide the eye.

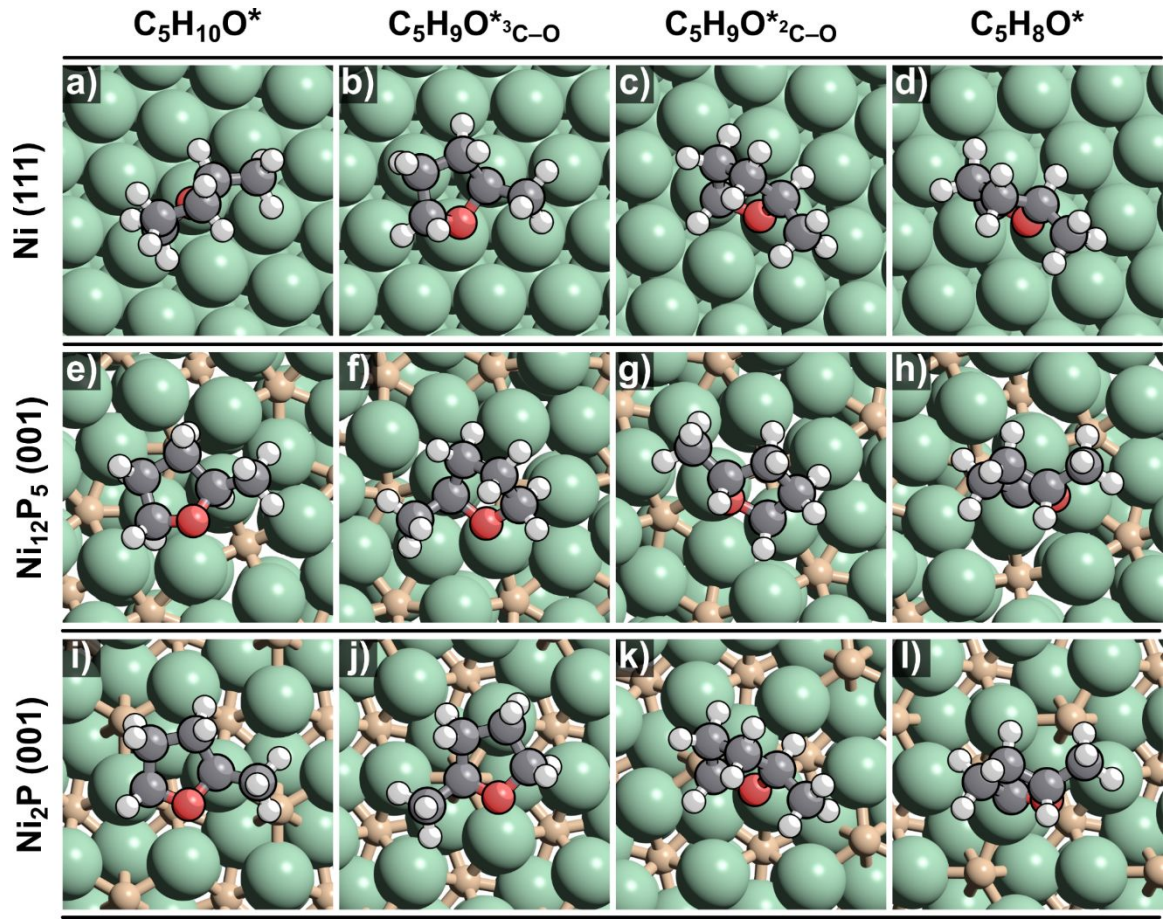

Figure S12. Top views for the DFT-predicted structures of the reactive intermediates ($C_5H_{10}O$*; C_5H_9O*$_{2C\text{-}O}$; C_5H_8O*; C_5H_9O*$_{3C\text{-}O}$) on Ni (a-d), $Ni_{12}P_5$ (e-h), and Ni_2P (i-l) using the RPBE functional.

S5. Isolated Species over Ni and Ni_2P

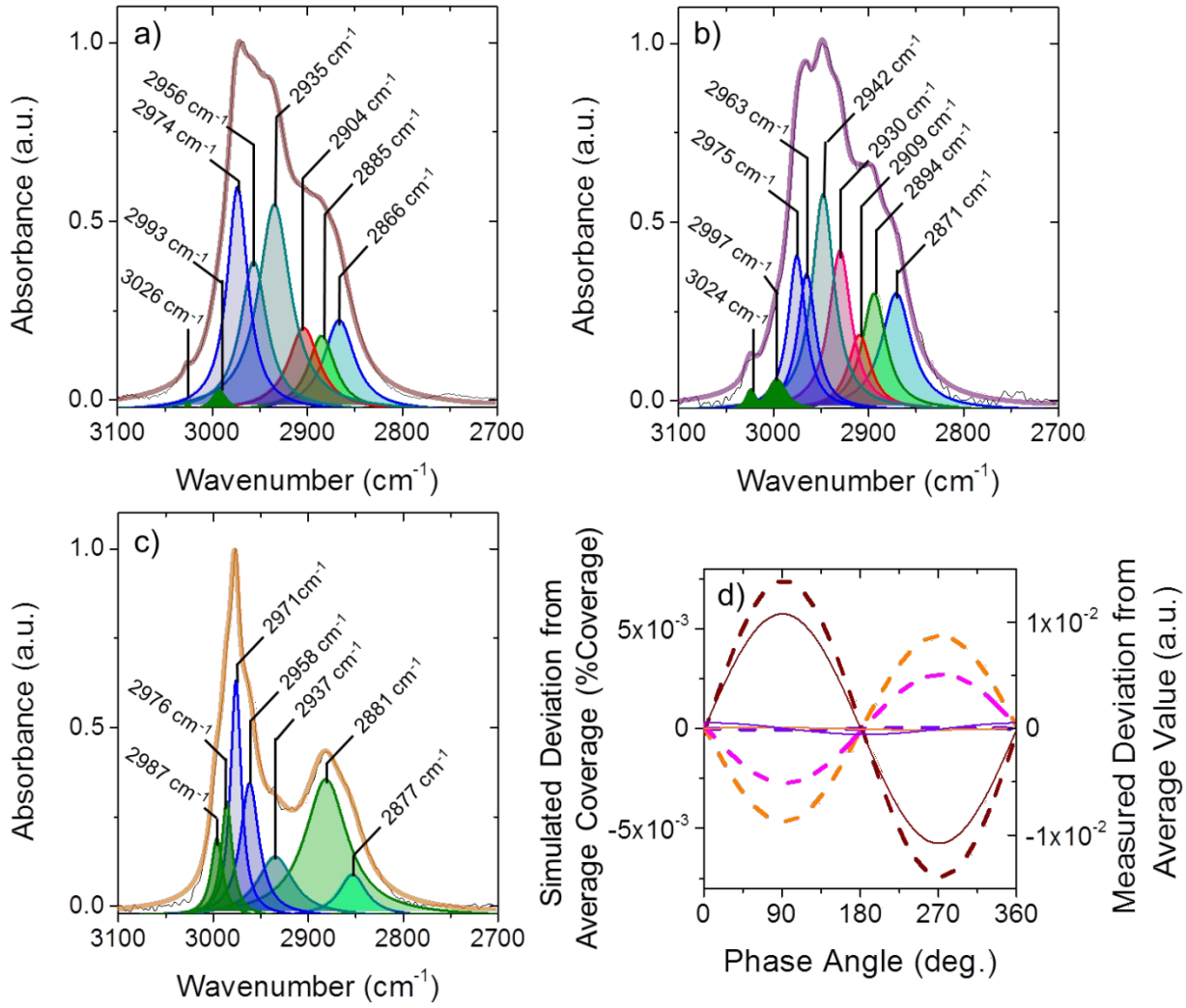

Figure S13 Spectra of independent reactive intermediates a) $C_5H_{10}O$* (brown); b) $C_5H_9O_{2C\text{-}O}$* (purple), and c) $C_5H_9O_{3C\text{-}O}$ * (orange) formed during modulation of [H_2] (2.5-84 kPa H_2, 12 kPa MTHF, 543 K, 1500 s period) over 12 nm Ni_2P extracted from phase domain spectra using MCR-ALS. Spectra fit to Lorentzian distributions that indicate individual C-H stretches ($\nu_a(CH_3)$ green; $\nu_s(CH_3)$ light green; $\nu_a(CH_2)$, blue; $\nu_{ap}(CH_2)$, teal; $\nu_s(CH_2)$, light blue; ν(CH) of ^{3}C, red; ν(CH) of ^{2}C, pink) which form the cumulative spectra (transparent thick line). d) Predicted (dashed) and measured (solid) deviations from average coverage of reactive intermediates ($C_5H_{10}O$*, brown; $C_5H_9O^*_{2C\text{-}O}$, purple; $C_5H_9O^*_{3C\text{-}O}$, orange; C_5H_8O*, pink) during modulation of H_2 pressure over Ni_2P (2.5-84 kPa, 12 kPa MTHF, 543 K, 1500 s period). The differential equations and estimated rate constants to calculate the predicted coverages are detailed in the Supporting Information Section S4 and Table S9.

The spectra in Figure S13a has the greatest measured change in coverage over 12 nm Ni_2P (Figure S13d), which indicates it is the MARI. Kinetic data determine $C_5H_{10}O$* is the MARI on Ni_2P,[8] and DFT optimized structures depict the MARI as $Ni_3(\eta^5\text{-}C_5H_{10}O^*)$ (laying parallel with the Ni_2P surface). The

intensity of $\nu_{CH2,ap}$(C-H) (~2940 cm^{-1}) to $\nu_{CH2,a}$(C-H) (~2970 cm^{-1}) is greater than in this species relative to the other two species on Ni_2P as more methylene groups are perturbed by the surface, which is consistent with $Ni_3(\eta^5\text{-}C_5H_{10}*)$. The absence of the ν_{CH}(C-H) at ~2910 cm^{-1} in the blue spectra matches the structure of $C_5H_9O*_{3C\text{-}O}$ that has lost one H at the ^{3}C leading to ^{3}C-O bond rupture. The spectral feature at ~2930 cm^{-1} in the spectra in Figure 13b indicates a second ν_{CH}(C-H) at the ^{2}C from the first dehydrogenation step in addition to the methyne group at the ^{3}C (~2910 cm^{-1}); thus, this spectra represents $C_5H_9O*_{2C\text{-}O}$.

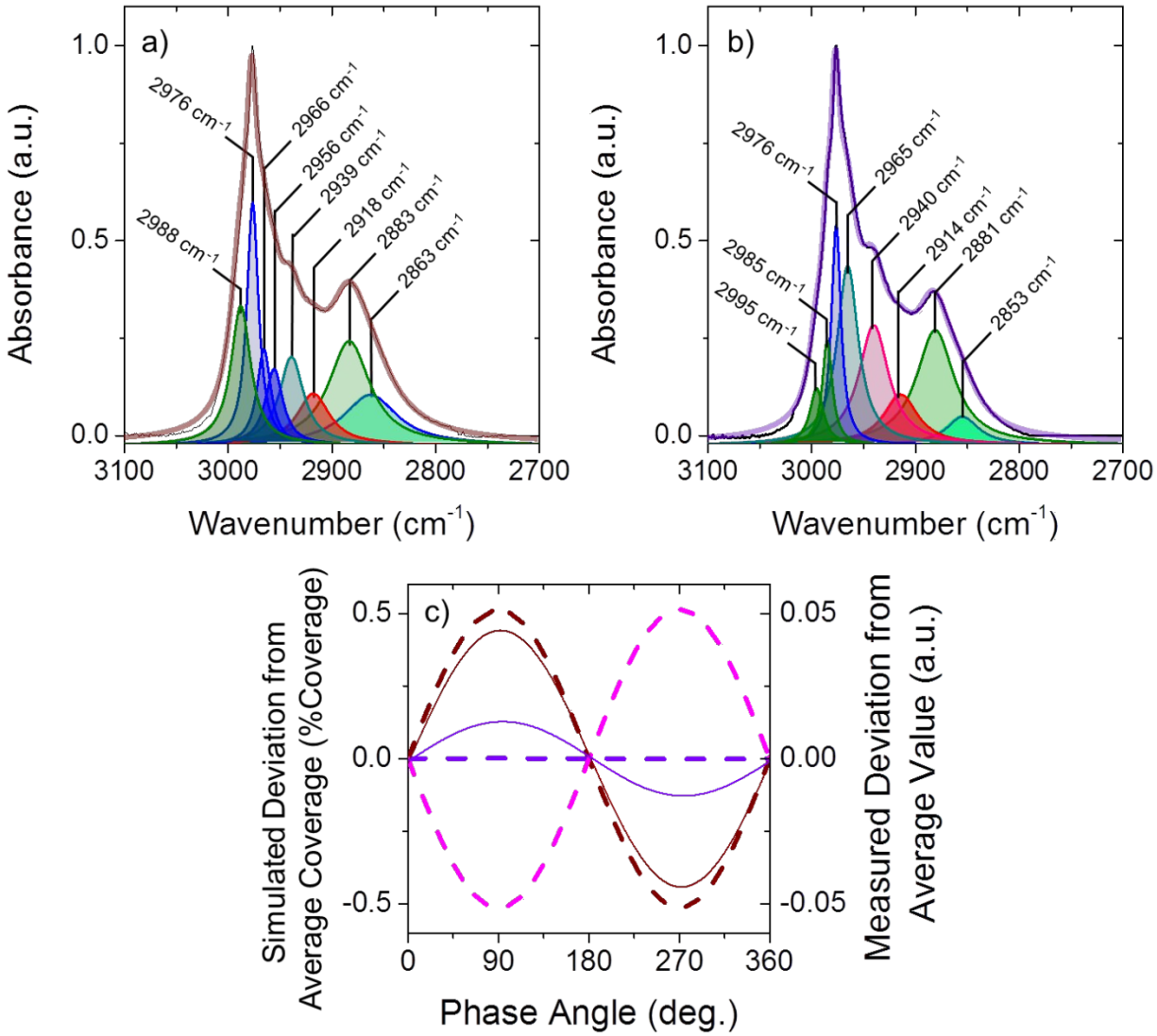

Figure S14 Spectra of independent reactive intermediates a) $C_5H_{10}O*$ (brown) and b) $C_5H_9O_{2C\text{-}O}*$ (purple) formed during modulation of [H_2] (2.5-84 kPa H_2, 12 kPa MTHF, 543 K, 700 s period) over 4 nm Ni_2P extracted from phase domain spectra using MCR-ALS. Spectra fit to Lorentzian distributions that indicate individual C-H stretches ($\nu_a(CH_3)$ green; $\nu_s(CH_3)$ light green; $\nu_a(CH_2)$, blue; $\nu_{ap}(CH_2)$, teal; $\nu_s(CH_2)$, light blue; ν(CH) of ^{3}C, red; ν(CH) of ^{2}C, pink) which form the cumulative spectra (transparent thick line). c) Predicted (dashed) and measured (solid) deviations from average coverage of reactive

intermediates ($C_5H_{10}O^*$, brown; $C_5H_9O^*_{2C\text{-}O}$, purple; $C_5H_8O^*$, pink) during modulation of H_2 pressure over Ni_2P (2.5-84 kPa, 12 kPa MTHF, 543 K, 700 s period). The differential equations and estimated rate constants to calculate the predicted coverages are detailed in the Supporting Information Section S4 and Table S9.

The spectra in Figure S14a has a greater relative ratio of $\nu_{CH2,ap}$(C-H) (2939 cm^{-1}) to $\nu_{CH2,a}$(C-H) (2976 cm^{-1}) in comparison to the spectra in Figure 14b. The ratio of asymmetric C-H stretching modes (2990-2960 cm^{-1}) to symmetric stretching modes (2880-2860 cm^{-1}) is greater for the brown spectra in Figure S14a, which indicates the plane of the furan ring changes orientation relative to the Ni surface such that the net z component of the C-H bonds in methyl and methylene groups is non-zero relative to the catalyst surface in the xy-plane as illustrated Figure S8. These observations suggest that the spectra in Figure 14a is the MARI ($C_5H_{10}O^*$) which has a perturbed methylene group directly oriented at the Ni surface as it binds perpendicular with the surface (Ni(μ^3-$C_5H_{10}O^*$)). The spectra Figure S14b does not have as many perturbed methylene groups as $C_5H_{10}O^*$ either from a dehydrogenation of the perturbed methylene or by a change in orientation. Since the ratio of asymmetric and symmetric methyl and methylene groups in the red spectra indicate the spectra in Figure 14b depicts a furan ring more tilted to the Ni surface than $C_5H_{10}O^*$, the spectra likely reflects $C_5H_9O^*_{2C\text{-}O}$. The measured change in coverage (Figure S14c) is also greater for $C_5H_{10}O^*$, which confirms that it is the MARI and consistent with previously reported kinetic data.[8]

Table S9 Intrinsic free energy barriers ($\Delta G^{\ddagger}$) for elementary steps described Scheme S1 and the calculated rate constants for simulated coverages in Figures S13d and S14c

Elementary Step	Ni		Ni_2P	
	$\Delta G^{\ddagger}$ (kJ mol^{-1})	Rate constant (s^{-1})	$\Delta G^{\ddagger}$ (kJ mol^{-1})	Rate constant (s^{-1})
1	5	$3.74*10^{12}$	5	$3.74*10^{12}$
-1	55	$6.32*10^{6}$	42	$1.03*10^{9}$
2a	83	$1.17*10^{7}$	97	$5.27*10^{3}$
-2a	52	$1.12*10^{8}$	60	$1.91*10^{7}$
3a	30	$1.47*10^{10}$	60	$1.91*10^{7}$
-3a	64	$7.88*10^{6}$	60	$1.91*10^{7}$
4a	66	$5.06*10^{6}$	95	$8.21*10^{3}$
2b	-[a]	-[a]	79	$2.84*10^{5}$
-2b	-[a]	-[a]	16	$3.27*10^{11}$
3b	-[a]	-[a]	74	$8.60*10^{5}$

[a]The ^{3}C-O bond rupture pathway was eliminated for these calculations as the DFT predicted rates are several orders of magnitude below ^{2}C-O bond rupture rates on Ni(111) and Ni(100).

S6. H_2 modulation over SiO_2 and comparisons with Ni, $Ni_{12}P_5$, and Ni_2P catalysts

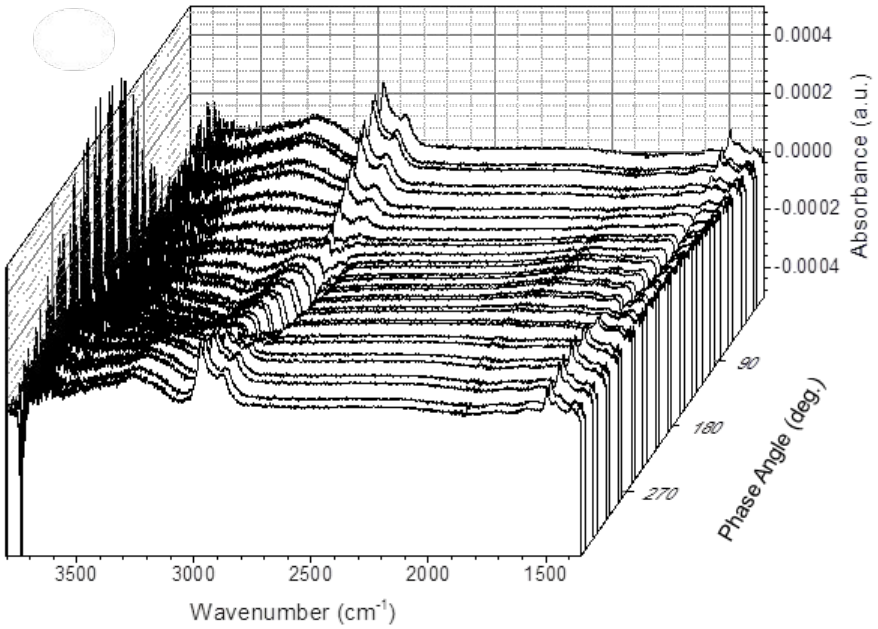

Figure S15 Phase resolved spectra during modulation of [H_2] (2.5-84 kPa H_2, 1500 s, 12 kPa MTHF, 543 K) over SiO_2.

The H_2 pressure changes appears to change the concentration of hydroxyl species and physisorbed MTHF on SiO_2 based on the change in intensity of the ν(C-H) (3000-2700 cm^{-1}), isolated SiOH (ν(O-H), ~3730 cm^{-1}) and adsorbed water (ν(O-H), 3000-3600 cm^{-1}). The concentration of MTHF is constant throughout these experiments, which means the observed changes in ν(C-H) are due to the physisorbed MTHF. The isolated SiOH groups are 180° out of phase with the ν(C-H) from MTHF (i.e., have a maximum intensity while the other reaches its minimum intensity), while the ν(O-H) of water are in phase with MTHF. The groupings of these spectral features suggests that MTHF physisorbs to the SiO_2 surface by replacing the hydroxyl groups or the hydroxyl groups dehydrate to form water on the SiO_2 surface as a result of different H_2 pressures.

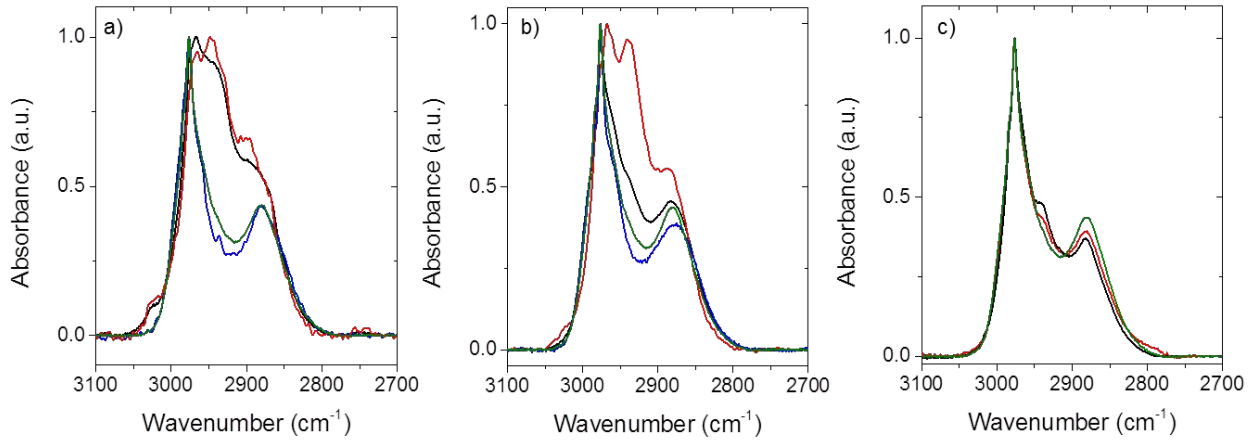

Figure S16 Spectra of independent reactive intermediates ($C_5H_{10}O$*, black; C_5H_9O*, red; C_5H_9O*', blue) formed during modulation of [H_2] (2.5-84 kPa H_2, 12 kPa MTHF, 543 K) over 12 nm Ni_2P (a, 1500 s), 10 nm $Ni_{12}P_5$ (b, 1200 s), 4 nm Ni (c, 700 s) and extracted from phase domain spectra using MCR-ALS. The green spectra reflect the species over SiO_2 during modulation of [H_2] (2.5-84 kPa H_2, 1500 s period, 12 kPa MTHF, 543 K).

Phase resolved spectra (Figure S15) that result from MES of H_2 pressure over SiO_2 are comprised of a single species that oscillates at the applied frequency (T = 1500 s). The species over SiO_2 that changes with H_2 pressure is not duplicated over the SiO_2 supported Ni, $Ni_{12}P_5$, or Ni_2P nanoparticles. Additionally, the isolated species on each catalyst (Ni, $Ni_{12}P_5$, and Ni_2P, Figure S16) have unique spectra, which affirms the assumption that the isolated spectra from MES experiments over Ni, $Ni_{12}P_5$, or Ni_2P catalysts reflect species bound to the Ni, $Ni_{12}P_5$, or Ni_2P surfaces and not SiO_2.

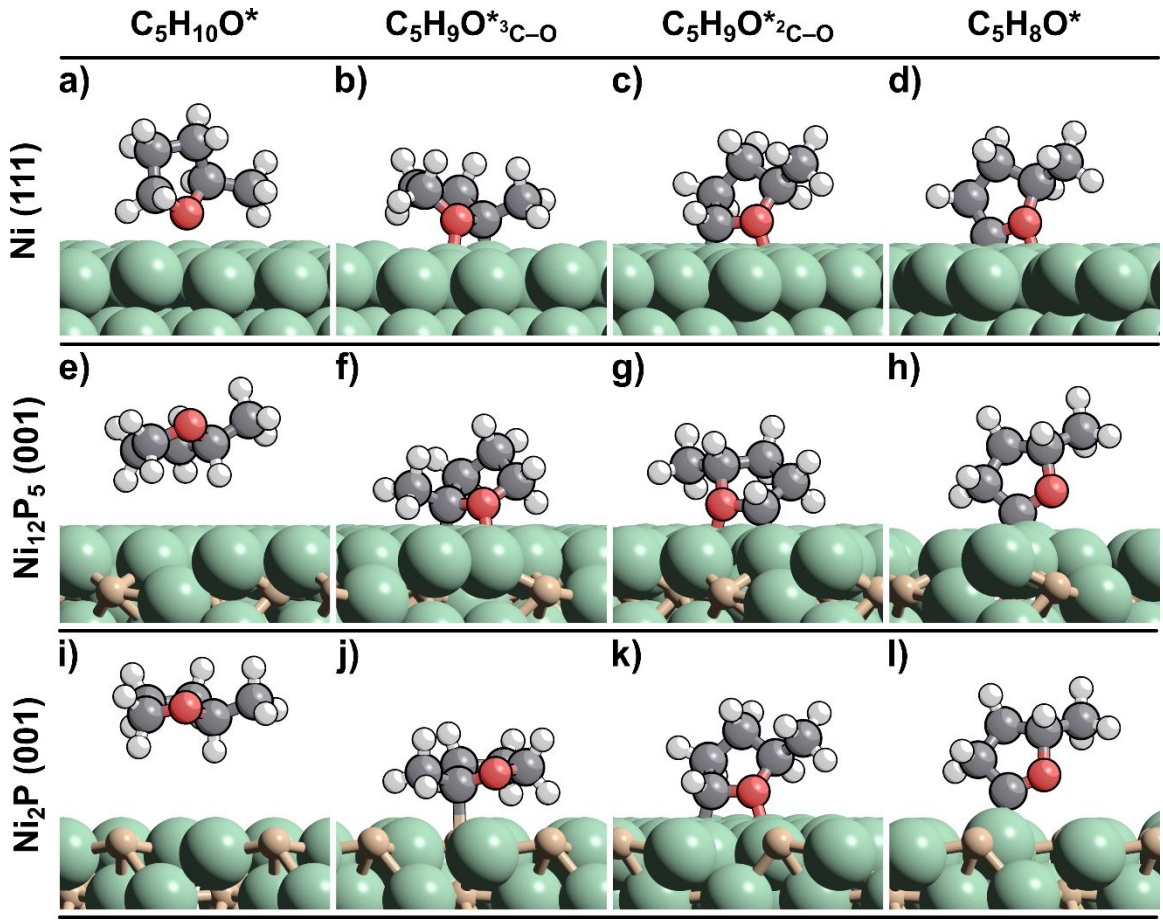

Figure S17. DFT-predicted structures of the reactive intermediates ($C_5H_{10}O^*$; $C_5H_9O^*_{2C\text{-}O}$; $C_5H_8O^*$; $C_5H_9O^*_{3C\text{-}O}$) on Ni (a-d), $Ni_{12}P_5$ (e-h), and Ni_2P (i-l) using the optB88-vdW functional.

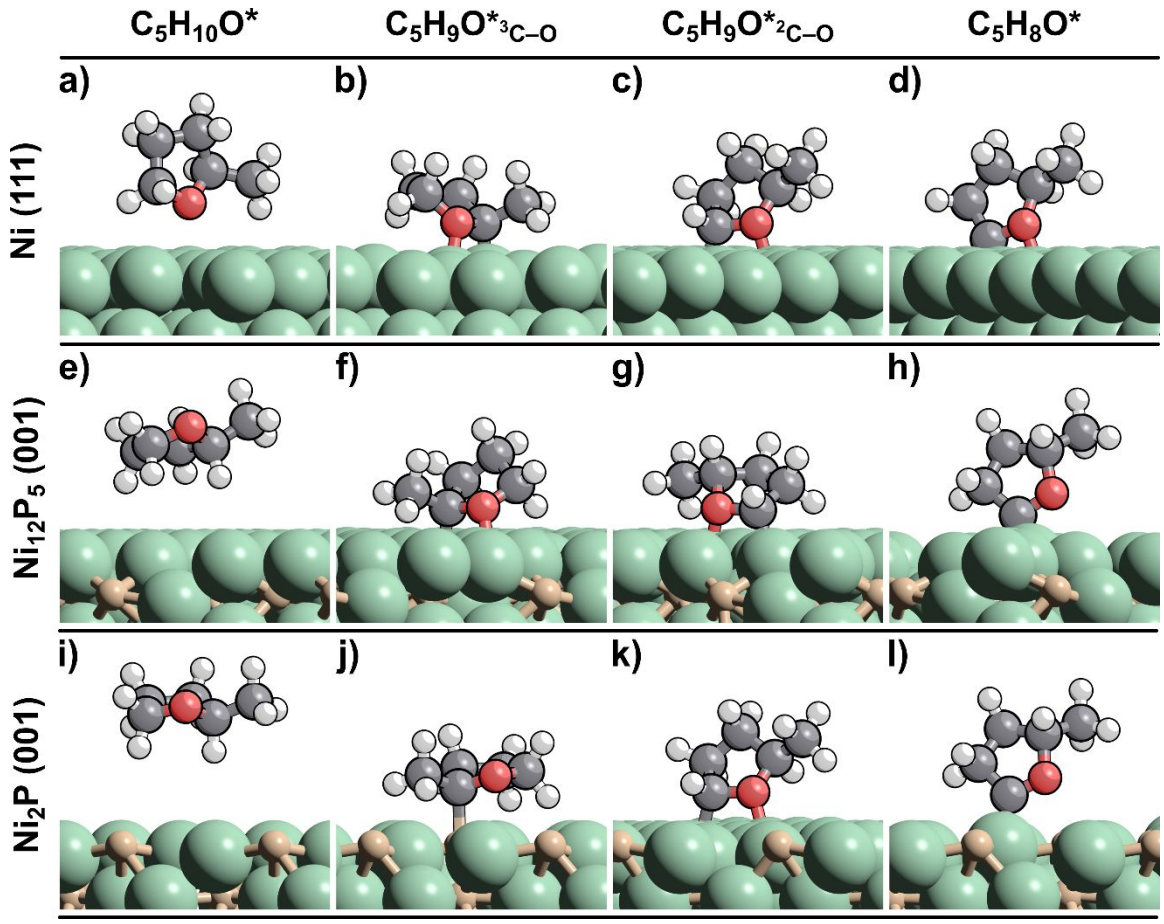

Figure S18. DFT-predicted structures of the reactive intermediates ($C_5H_{10}O^*$; $C_5H_9O^*_{2C\text{-}O}$; $C_5H_8O^*$; $C_5H_9O^*_{3C\text{-}O}$) on Ni (a-d), $Ni_{12}P_5$ (e-h), and Ni_2P (i-l) using the optB86-vdW functional.

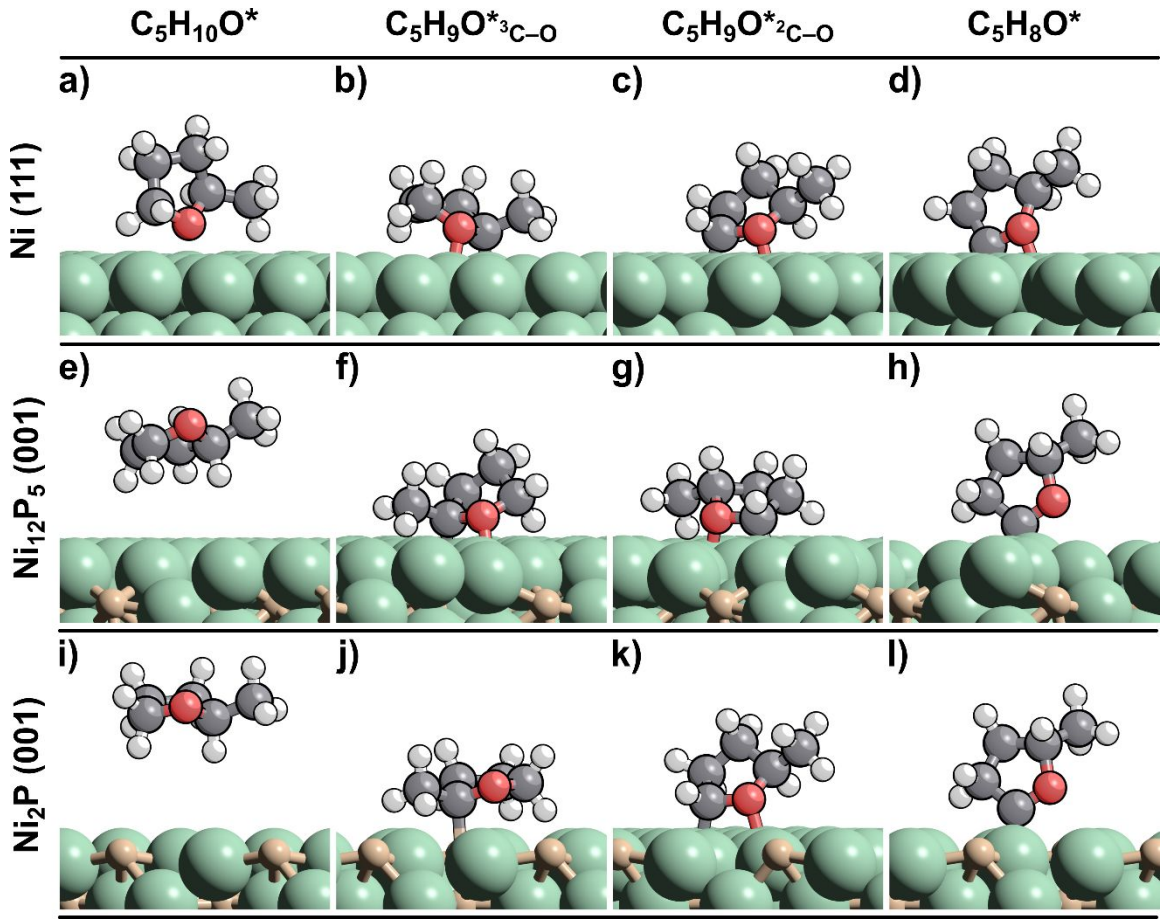

Figure S19. DFT-predicted structures of the reactive intermediates ($C_5H_{10}O^*$; $C_5H_9O^*_{2C\text{-}O}$; $C_5H_8O^*$; $C_5H_9O^*_{3C\text{-}O}$) on Ni (a-d), $Ni_{12}P_5$ (e-h), and Ni_2P (i-l) using the RPBE-D3BJ functional.

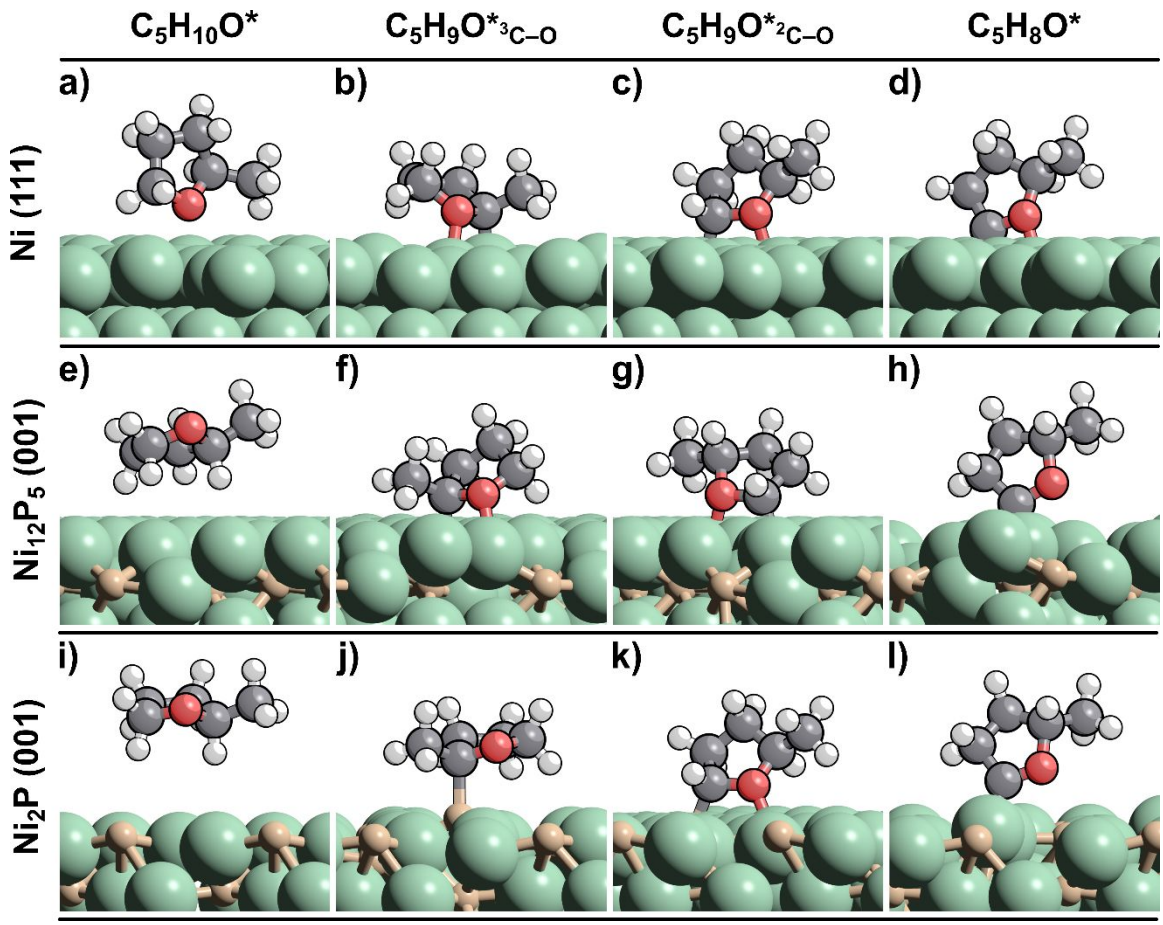

Figure S20. DFT-predicted structures of the reactive intermediates ($C_5H_{10}O^*$; $C_5H_9O^*_{2C\text{-}O}$; $C_5H_8O^*$; $C_5H_9O^*_{3C\text{-}O}$) on Ni (a-d), $Ni_{12}P_5$ (e-h), and Ni_2P (i-l) using the vdW-DF2 functional.

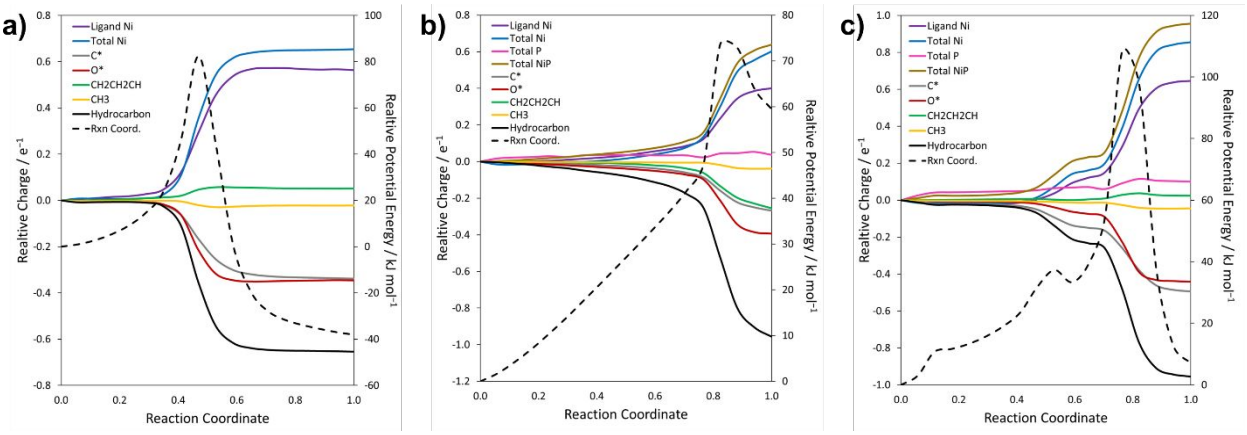

Figure S21. Reaction coordinate diagram for ^{2}C–O cleavage in $C_5H_8O^*_{2C–O}$ showing relative electronic energy (kJ mol^{-1}, dashed lines) and relative charges (in e^-, solid lines) normalized by the reactants over a) Ni(111), b) $Ni_{12}P_5$(001), and c) Ni_2P(001).

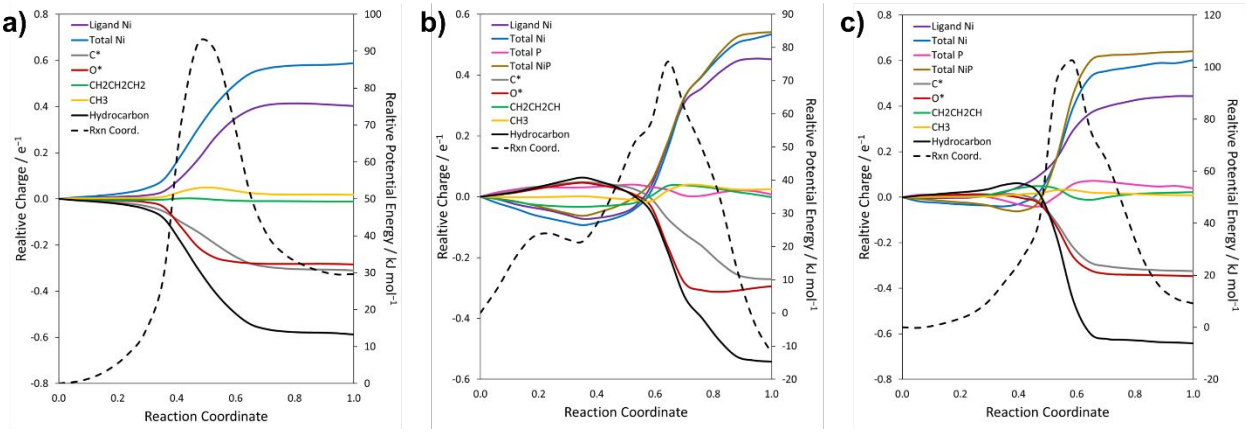

Figure S22. Reaction coordinate diagram for ^{3}C–O cleavage in $C_5H_9O^*_{3C–O}$ showing relative electronic energy (kJ mol^{-1}, dashed lines) and relative charges (in e^-, solid lines) normalized by the reactants over a) Ni(111), b) $Ni_{12}P_5$(001), and c) Ni_2P(001).

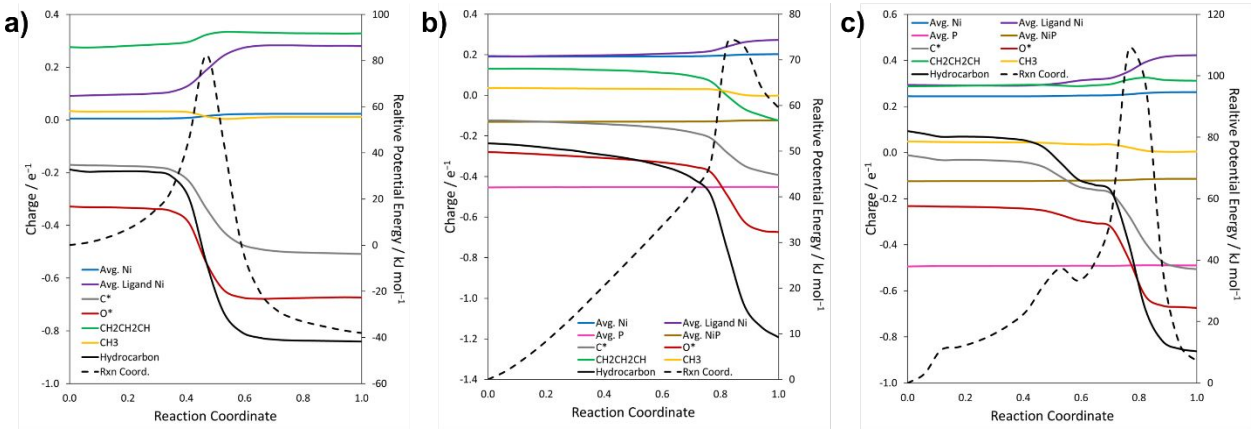

Figure S23. Reaction coordinate diagram for $^{2}C–O$ cleavage in $C_5H_8O^*_{2C–O}$ showing relative electronic energy (kJ mol^{-1}, dashed lines) and partial charges (in e^-, solid lines) over a) Ni(111), b) $Ni_{12}P_5(001)$, and c) $Ni_2P(001)$.

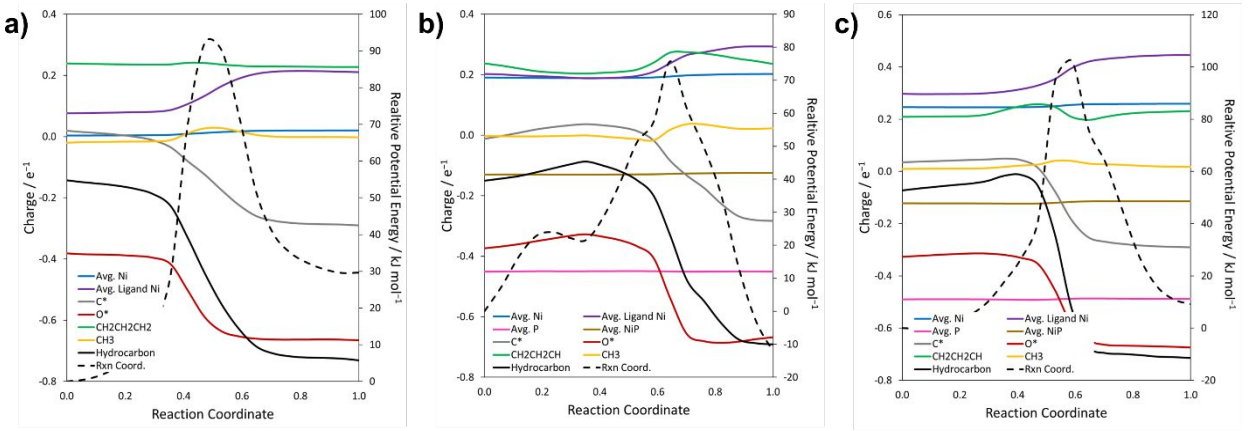

Figure S24. Reaction coordinate diagram for $^{3}C–O$ cleavage in $C_5H_9O^*_{3C–O}$ showing relative electronic energy (kJ mol^{-1}, dashed lines) and partial charges (in e^-, solid lines) over a) Ni(111), b) $Ni_{12}P_5(001)$, and c) $Ni_2P(001)$.

References

(1) Yang, M.; Somorjai, G. A. *J. Am. Chem. Soc.* **2004**, *126*, 7698.
(2) Bratlie, K. M.; Somorjai, G. A. *J. Phys. Chem. C* **2007**, *111*, 6837.
(3) Ilharco, L. M.; Garcia, A. R.; daSilva, J. L. *Surf. Sci.* **1997**, *371*, 289.
(4) Aliaga, C.; Tsung, C. K.; Alayoglu, S.; Komvopoulos, K.; Yang, P. D.; Somorjai, G. A. *J. Phys. Chem. C* **2011**, *115*, 8104.
(5) del Arco, M.; Gutierrez, S.; Martin, C.; Rives, V. *PCCP* **2001**, *3*, 119.
(6) Thompson, C. M.; Carl, L. M.; Somorjai, G. A. *J. Phys. Chem. C* **2013**, *117*, 26077.
(7) Cho, A.; Kim, H.; Iino, A.; Takagaki, A.; Oyama, S. T. *J. Catal.* **2014**, *318*, 151.
(8) Witzke, M. E.; Almithn, A.; Coonrod, C. L.; Hibbitts, D. D.; Flaherty, D. W. *ACS Catal.* **2018**, *8*, 7141.